RSC Advances

PAPER

View Article Online
View Journal | View Issue

Cite this: *RSC Adv.*, 2025, **15**, 5060

Personalised 3D-printed bioactive peek bone plate scaffold for treating femoral defects†

Wenquan Zhang,[a] Dayou Shi,[c] Shirui Huang,[c] Shaochuan Li,[c] Min Zeng[b] and Yanming Wei *[a]

Fractures affect millions of individuals worldwide, particularly those with osteoporosis, and often require rigid fixation for proper healing. Although traditional metal bone plates are effective, they are limited by their stiffness and inability to conform precisely to anatomical structures, leading to complications such as stress shielding and delayed healing. In this study, we utilized computer-aided design (CAD) combined with reverse engineering to develop a 3D bone plate scaffold model that perfectly matches the contours of the rabbit femur. Additionally, we employed fused deposition modeling (FDM) 3D printing to fabricate a customized polyetheretherketone (PEEK) bone plate scaffold based on the model, designed to match individual bone structures and reduce rigidity-related issues. To enhance the bioactivity of the PEEK scaffold surface, we applied plasma spraying technology to coat it with bioactive materials, including nanohydroxyapatite (HA), tantalum (Ta), and titanium (Ti). The results showed that the HA coating contained 48.06% calcium (Ca) and 16.47% phosphorus (P) and the Ti coating contained 82.32% Ti. *In vitro* studies showed that the bioactive scaffold effectively promoted the proliferation and differentiation of osteogenic mesenchymal stem cells, with a cell survival rate greater than 93.86%. Moreover, *in vivo* results from the rabbit femoral defect model showed that the bioactive scaffolds significantly accelerated bone tissue healing, with HA-coated PEEK scaffolds exhibiting exceptional bone regeneration potential. This study proposes a comprehensive strategy for customizing bone plate scaffolds, which holds significant promise for personalized precision medicine.

Received 23rd October 2024
Accepted 26th January 2025

DOI: 10.1039/d4ra07573k

rsc.li/rsc-advances

1. Introduction

Fractures represent a common bone tissue injury with a global incidence of about 445 million,[1] and are prone to occur in people with osteoporosis or low bone density, such as children and the elderly. With the rapid development of the global aging population, the incidence of new fractures has increased by 33.4% worldwide. Adults also suffer from fractures due to accidents such as car accidents and falls. Among all the parts where fractures occur, the incidence of fractures at the farthest ends of the limbs is the highest, such as the thigh and calf.[2,3] Fractures seriously affect the quality of life of patients and may cause disability, loss of independence, or even death, with the disability rate caused by fractures reaching 25.8 million per year.[1,4]

Bone tissue has a strong regenerative ability, but most fracture sites require rigid fixation, especially load-bearing sites such as the limbs. Clinically, bone plates are an excellent choice for fixing fracture sites, connecting the fracture ends to promote bone healing. However, traditional steel plates cannot perfectly match the physiological bone structure due to limited size and shape. During the operation, surgeons have to bend and adjust them, resulting in extended operation time, and slightly mismatched shapes may cause a delay in healing and increase the risk of complications.[5] Therefore, developing a design strategy for bone plate holders customized according to anatomical shapes and fracture types is crucial in the development of implantable medical devices.

Traditional metal implants made of standard materials such as titanium or stainless steel have too high stiffness relative to bone tissue, which may cause excessive conformity of the bone plate after implantation while providing stability to the fracture site.[6,7] Excessive concentrated stress distribution can lead to implant wear, bone resorption caused by stress shielding, and even hinder the formation of callus to delay healing.[8] Relatively low bone implant materials have attracted widespread attention in the design of fixed implants.[9] Polyetheretherketone (PEEK) is one of the important engineering plastics with wear resistance and corrosion resistance.[10,11] Due to its excellent

[a]*Institute of Traditional Chinese Veterinary Medicine, College of Veterinary Medicine, Gansu Agricultural University, Lanzhou, Gansu Province 730070, China. E-mail: weiym@gsau.edu.cn*

[b]*Inuoer Pet Hospital, Foshan, Guangdong Province 528299, China*

[c]*College of Veterinary Medicine, South China Agricultural University, Guangzhou, Guangdong Province 510000, China*

† Electronic supplementary information (ESI) available. See DOI: https://doi.org/10.1039/d4ra07573k

biocompatibility and elastic modulus close to that of cortical bone, about 3–4 GPa, PEEK is widely used in orthopedic implants and prostheses.[12] In addition, the plasticity of PEEK material allows it to be prepared into any morphology that conforms to the bone structure through various additive manufacturing methods.[13]

Fused deposition modeling (FDM) is an extrusion three-dimensional (3D) printing technology that is widely used in the development of medical devices with specific structures due to its simple operation and cost-effectiveness.[14] FDM can melt and extrude PEEK to stack layers and accurately print PEEK implants with different morphologies and structures according to product design.[15] Hyung-Jin Chung *et al.* prepared a PEEK locking compression version that matched the mechanical properties of the fracture site through an FDM 3D printer.[16] In this study, we selected PEEK material and FDM 3D printing technology to realize the customized bone plate design strategy. Notably, osseointegration is beneficial to the growth of bones around orthopedic implants.[17] However, the hydrophobicity and chemical inertness of PEEK materials and the smooth surface of PEEK implants limit its performance in osseointegration, while the composition and morphology of the implant surface greatly affect osseointegration.[18] We coated the surface of PEEK bone plate scaffolds with bioactive materials including nano-hydroxyapatite (HA), tantalum (Ta), and titanium (Ti) by plasma spraying technology to prepare bioactive PEEK bone plate scaffolds.[19,20]

Given the limitations of traditional plates, we developed a bone plate scaffold that is precisely customized according to the personal bone structure. We used New Zealand rabbits as research subjects and scanned them by computed tomography (CT) to collect femoral data. Next, we designed and constructed a 3D model of the bone plate bracket that perfectly fits the femoral contour through the reverse engineering software Geomagic Studio 12 (64 bit, Raindrop Geomagic, Inc., USA) and UG NX 10.0 software (Unigraphics NX). Then, we tested the stress distribution of the 3D model of the bone plate scaffold by finite element analysis and the results showed that the 3D model fully met the mechanical performance requirements of a bone plate, and prepared a bioactive PEEK bone plate scaffold based on the 3D model.[21–23] To evaluate the osteogenic properties of the bioactive bone plate scaffolds *in vivo*, we constructed the rabbit bone perforation defect model and implanted the scaffolds. CT results and histochemical staining results showed that the bioactive bone plate scaffolds accelerated bone regeneration and generated mature bone bridging the defect site. Moreover, the HA-PEEK bone plate showed outstanding bone tissue healing due to its excellent bioactivity and osteoinductivity. This study proposed a comprehensive strategy for customized bone plate scaffolds for fractures and is expected to be further developed for more complex bone structures and sites.

2. Materials and methods

2.1 Materials

PEEK was purchased from Yimai Intelligent Co., Ltd in Dongguan, China. Ta was purchased from Hunan Print Medical Instrument Co., Ltd. Ti was purchased from Zunyi Boyu Titanium Material Co., Ltd. HA was purchased from Nanjing Epre Nanomaterials Co., Ltd. α-MEM medium (12571063), fetal bovine serum (FBS, Gibco, 12664025) and penicillin–streptomycin (Gibco, 15140122) were purchased from Thermo Fisher Scientific China Co., Ltd. Alizarin red S staining solution (G1038-100ML) was purchased from Wuhan Servicebio Technology CO., Ltd. TRAP/ALP stain (294-67001) was purchased from Wako Pure Chemical Industries, Ltd. Cell Counting Kit-8 (CCK-8, BA00208) was purchased from Beijing Bioson Biotechnology Co., Ltd.

2.2 Three-dimensional design of bone plate scaffold

2.2.1 CT data acquisition and processing. All animal procedures used in this study were specifically approved by the Animal Ethics and Use Committee of Gansu Agricultural University, and animal welfare requirements were met. A male New Zealand white rabbit (4 kg, 12 months old) was used for femur data collection. The rabbit was healthy and housed in a 25 °C breeding room with a 12 hours light–dark cycle. The rabbit was anesthetized by injection of 30 mg of Sutent 50. The rabbit was scanned from the acetabulum to the distal femur by CT (OMATOM Definition Flash, dual-source 128-slice) in the supine position. The scanning parameters were set as scanning current 95 mA, scanning voltage 120 kV, scanning image slice thickness 0.6 mm, 512 × 512 pixels, and scanning frame tilt 0°. Then, the rabbit femur data were processed by Mimics Research 21.0.

2.2.2 Surface editing of a rabbit femur model. To obtain a more suitable femoral anatomical shape, we performed surface editing on the rabbit femur model using Geomagic Studio 12. The rabbit slice model file was converted into a solid file for finite element simulation. The processing in Geomagic Studio 12 is shown in Fig. 1.

2.2.3 Design and assembly of plate scaffolds and screws. To design a suitable implantable bone plate bracket, we designed the entity file of the rabbit femur model through UG NX 10.0. The curve of the femoral surface was extracted and the bone plate maintained the overall curved shape consistent with the direction of the femur, as shown in Fig. 2. The part where the bone plate fits the bone was also designed as a curved surface.

In order to ensure the appropriate stiffness of the internal fixation system, we designed the basic model of hole type difference and screws based on this method through UG (Fig. 2 and 3).

The designed splint model, femoral model and screw model were assembled. After the splint was adjusted to the appropriate position of the femur, the size of the model was adjusted until it reached the optimal state.

2.2.4 Finite element analysis. To simulate the stress distribution of the bone plate bracket under a certain pressure, the femoral splint we designed was subjected to finite element analysis through ANSYS Workbench 18.0 (Swanson Analysis Systems, Inc, USA). The model was imported from UG NX into ANSYS Workbench with a ten-node tetrahedral mesh and cell

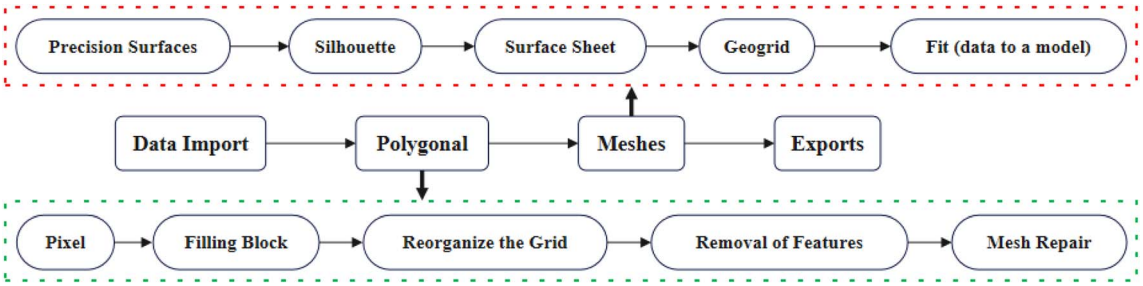

Fig. 1 Surface treatment process of rabbit femur model.

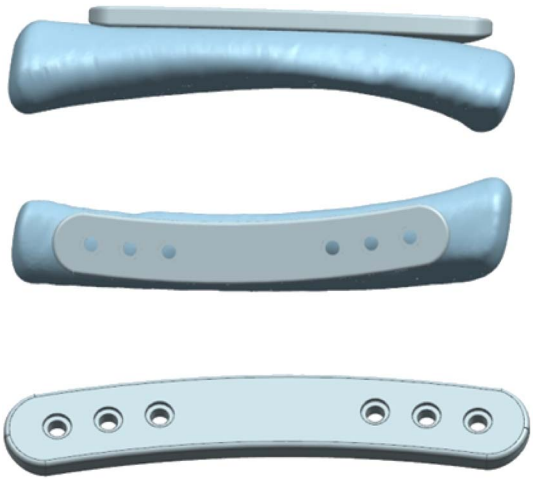

Fig. 2 Design of the graft plate scaffold model.

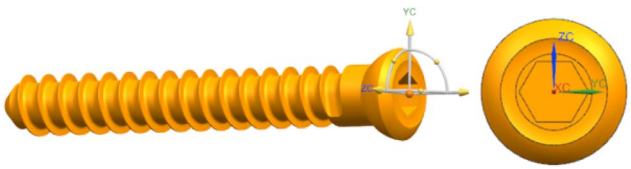

Fig. 3 Design of the splice screw model.

size of 0.2 mm. The material properties (elastic modulus (E) and Poisson's ratio (μ)) were set to $E = 4$ GPa, $\mu = 0.3$. To simulate the use of an actual femoral bone plate, the bottom boundary condition was set to be completely fixed and a force of 1.5 times the body weight of a test rabbit (50 N) was loaded on the top.[24]

2.3 Preparation of 3D printed bone plate scaffolds

We used PEEK to prepare 3D printed bone plate scaffolds. PEEK is different from ordinary 3D printing polymer materials, which require higher printing conditions due to the high melting point. Table 1 shows the material properties of PEEK.

The PEEK plate scaffold was prepared by an FDM 3D printer (Dongguan Yimai Intelligent Technology Co., Ltd. High Temperature 3D Printer Series MAGIC-HT-L). Table 2 shows the 3D printing parameters. The nozzle temperature was set to 450 °C, which was higher than the melting point of PEEK to facilitate extrusion speed and layer sedimentation. To reduce thermal shrinkage, the hotbed temperature was set to 150 °C, close to the glass transition temperature of PEEK. To support thermal shrinkage and molding layers, the cavity temperature was set to 90 °C. The size of the PEEK plate scaffold is 310 × 310 × 480 mm^3.

Table 1 Physical and chemical properties of PEEK used for 3D printed bone plate scaffolds

Performances	Unit	Rating
Densities	g cm^{-3}	1.29
Tensile strength	MPa	100
Bending strength	MPa	170
Bending modulus	MPa	4200
Melting point	°C	334

2.4 Preparation and characterization of bioactive bone plate scaffold

To enhance the bioactivity of the surface of the scaffolds, we plasma sprayed the PEEK bone plates. First, we sandblasted the PEEK plate to enhance the adhesion of the coating. The surface of the plate was roughened by high-speed spraying of brown corundum at a pressure of 0.4 MPa. Three different materials (metal tantalum powder, nano-hydroxyapatite, and metal titanium powder) were made into bioactive coatings separately through a plasma spray system (CL WI-091, GTV, Germany). The study has reported that plasma surface treatment will not cause

Table 2 3D printing parameters of PEEK bone plate scaffolds

Process parameters	Unit	Set value
Printing temperature	°C	380
Material box temperature	°C	60
Chamber temperature	°C	120
Hot bed temperature	°C	100
Printing speed	mm s^{-1}	45
Filling degree	%	100
Filling pattern	—	Tetrahedron
Wall thickness	mm	0.4
Layer thickness	mm	0.2
Line width	mm	0.2

Table 3 Parameters of active coatings prepared by atmospheric plasma spraying

Parameters	Unit	Ta	Ti	HA
Nitrogen (Ar)	slpm	45	45	45
Hydrogen (H_2)	slpm	10	8	4.5
Carrier gas	L min^{-1}	4	3	3
Powder feeding rate	g min^{-1}	10	10	15
Spraying distance	mm	200	200	140
Gun movement speed	mm s^{-1}	1000	1000	1000
Power	kW	40	40	30

significant changes in the crystallinity and properties of PEEK materials.[25] Before plasma spraying, metal tantalum powder, nanohydroxyapatite and metal titanium powder were placed in a 90 °C oven for 24 h. The initial powders are shown in Fig. S1.† The specific spraying parameters are shown in Table 3. During the coating process, we carefully controlled the process temperature to prevent any thermal degradation or warping of the PEEK material. The temperature was monitored and maintained at a level that would not adversely affect the mechanical properties of the PEEK substrate. To make better use of the bioactive coating, we limited the spraying area to the fracture in the middle of the bone plate. At the same time, we designed the porous structures to facilitate the adhesion and proliferation of osteoblasts.

The surface elements of Ta-coated, HA-coated, and titanium-coated bone plate scaffolds (Ta-PEEK, HA-PEEK and Ti-PEEK) were detected by X-ray diffractometer (Ultima IV, Rigaku Corporation, Japan). Then, the microscopic morphology of the scaffolds was observed by scanning electron microscopy (SEM, XL-30E, Philips Photonics, The Netherlands).

The mechanical properties of PEEK bone plates were tested by three-point bending test.[26] PEEK bone plates were prepared according to the above method and tested by universal testing machine according to the requirements of GB/T9341-2000. The center line of the sample was pressed at a speed of 5 mm min^{-1} at 25 °C. The maximum bending force and elastic modulus of the sample were recorded.

2.5 Cytocompatibility evaluation of bioactive bone plate scaffolds

The cytotoxicity of bioactive bone plate scaffolds to rBMSC was tested by CCK-8 assay. α-MEM medium was added with 10% FBS and 1% penicillin–streptomycin to prepare a complete medium for the culture of rBMSCs. rBMSC were first inoculated in 96 well plates at a density of 5000 cells per well and were cultured in a CO_2 incubator 24 h. Ta-PEEK, HA-PEEK and Ti-PEEK scaffolds were sterilized and immersed in the complete culture medium at a ratio of 0.1 g mL^{-1}. The extracts of the scaffolds were obtained after 24 h of incubation. Subsequently, the original medium was aspirated and replaced with the extracts of different groups. After incubation for a specific time (24 h, days 2 and 3), cells were washed with PBS. 100 μL of fresh medium (containing 10% CCK-8) was added to each well and the cells were incubated in the incubator. The absorbance of the cells was detected at 450 nm by a microplate reader. The relative proliferation rate (RPR%) of the cells was calculated by the formula (1).

$$\mathrm{PRP}\ (\%) = (A_1 - A_b)/(A_n - A_b) \times 100\% \quad (1)$$

where A_1 was the absorbance of the experimental group, A_b was the absorbance of the blank group, and A_n was the absorbance of the negative control.

2.6 Osteogenesis evaluation of bioactive bone plate scaffolds *in vitro*

To evaluate the osteogenic efficacy of the scaffolds, we co-cultured the extracts of bioactive bone plate scaffolds with rBMSCs and observed the mineralized nodules of rBMSCs. The extracts of PEEK, Ta-PEEK, HA-PEEK and Ti-PEEK were prepared as described above. rBMSCs were added to 24 well plates at 30 000 cells per well and cultured for 24 h in an incubator (5% CO_2, 37 °C). The cells were washed and the extracts of different groups (control, PEEK, Ta-PEEK, HA-PEEK and Ti-PEEK) were added to the wells for co-culture. The extracts were changed every 1–2 days until 14 days. The cells were fixed for 15 min with 1% paraformaldehyde solution. Then, the cells were washed and stained with Alizarin Red S solution. After 10–15 min, the cells were washed and observed under a microscope (Mingmei, MF50). In addition, the expression of ALP of rBMSCs was also observed. rBMSCs were fixed with pre-cooled 1% paraformaldehyde solution after 14 days of culture. Then, the cells were washed and ethanol/acetone (50 : 50 v/v) permeabilization solution was added. rBMSCs were placed in a −20 °C refrigerator for 1 min and then washed. ALP staining solution was added to rBMSCs and incubated for 15–60 min. After washing, the stained rBMSCs were observed. ImageJ-win64 software was used to measure the average gray value (IntDen/Area) of ALP staining and alizarin red staining.

2.7 Osteogenesis evaluation of bioactive bone plate scaffolds *in vivo*

New Zealand rabbits, 3 months-old female rabbits weighing 2.20–2.80 kg, were used for bone defect modeling. All New Zealand rabbits were provided by the Experimental Animal Center of Southern Medical University and were adaptively raised for 1 week before surgery. The temperature of the breeding room was 25 °C and the lighting was 12 hours of light–dark alternation. All experimental operations and surgical procedures were performed by the same experimental research team.

The experimental rabbits were fixed by a rabbit fixator and anesthetized by intraperitoneal injection of 10% chloral hydrate. At the same time, to prevent death caused by overdose of anesthesia, the vital signs of the rabbits were closely observed for changes in corneal reflex, breathing and chest rise and fall, and respiratory movement. When anesthesia took effect, the rabbits were fixed on the operating table with a bandage and the rabbits' applanation to the buttocks were shaved with a razor and depilatory cream. After disinfection, the distal limbs were wrapped with a sterile elastic bandage. The anterolateral surgical route

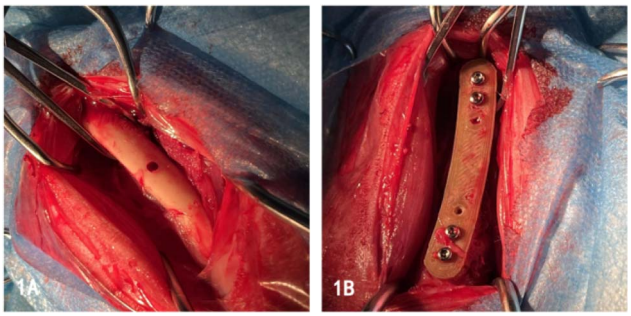

Fig. 4 Bone plate scaffold implantation surgery.

was selected and the skin and subcutaneous fascia of the line connecting the greater trochanter to the patella were incised. Next, the associated muscles of the femur were stripped to expose the lateral femoral metaphysis of the rabbits. A bone trephine was used to vertically drill a hole in the lateral metaphysis of the rabbit femur to create a bone perforation defect with a diameter of 7 mm and a depth of 10 mm. Each group of materials (control, PEEK, Ta-PEEK and HA-PEEK) were implanted into the corresponding defect area (Fig. 4). Then, the muscles, subcutaneous tissues and skin were sutured sequentially with 3-0 PGA absorbable sutures. The rabbits' wounds were disinfected with iodine and the rabbits were housed in single cages. The wound healing and eating habits of the rabbits were closely observed.

Fresh whole blood of rabbits was collected through the ear vein at 4, 8, and 12 weeks after surgery. Fresh whole blood was centrifuged (3500 rpm) for 15 min to obtain serum. Serum calcium and ALP levels were measured by blood biochemical analyzer. In addition, rabbits were sacrificed at 4, 8, and 12 weeks by air injection through the ear vein. The skin of the rabbits was incised along the original surgical incision and the muscles were peeled off layer by layer. The bone tissue of the defect area was removed and fixed by paraformaldehyde solution. The removed femoral tissue was subjected to X-ray examination. The detection conditions were voltage 45 kV, current 100 mA, exposure time 20 ms, and projection distance 10 cm. The new bone tissue areas (proximal, distal, and middle) of the rabbits were observed and the spatial bone pixel value was measured using a TOSHIBA DRX 3724HD digital imaging system. Furthermore, the bone tissue was subjected to hematoxylin–eosin (H&E) and Masson staining. The fixed tissue samples were placed in EDTA decalcification solution for decalcification. The decalcification solution was changed every 3 days until the bone tissue could be pierced by a fine needle. The decalcified bone tissue samples were paraffin-embedded and sectioned. The paraffin sections were stained with H&E stain and Masson stain, respectively. The stained sections were observed by microscope and the new bone formation rate was quantitatively counted using Image-Pro-Plus software.

2.8 Statistical analysis

All experiments were performed with a sample size of more than three and all experimental results are expressed as mean ± standard deviation. All quantitative and statistical results were analyzed by one-way analysis of variance. P values less than 0.05 were considered statistically significant ($^*p < 0.05$).

3. Results and discussion

3.1 Finite element analysis of bone plate scaffold model

Traditional bone grafts are mainly produced by casting or subtractive manufacturing, which lacks the consideration of individual bone differentiation. One of the advantages of 3D printing is that it can be used to personalize the implant prosthesis according to the bone data of an individual. Therefore, we scanned the rabbit femur through CT and used Mimics software to perform the 3D reconstruction (Fig. 5). Then, we used Geomagic Studio12 software to fill the holes on the surface of the 3D model, smooth it and accurately curve it. After editing and optimizing the surface of the 3D model, we obtained the ideal surface model (Fig. 6). Based on this, we designed a matching bone plate scaffold model and screw model (Fig. 7).

We performed finite element analysis on the designed 3D bone plate scaffold model to observe the stress distribution of the implant. The stress distribution images (Fig. 8) showed that the ends and edges of the plate exhibit higher numerical

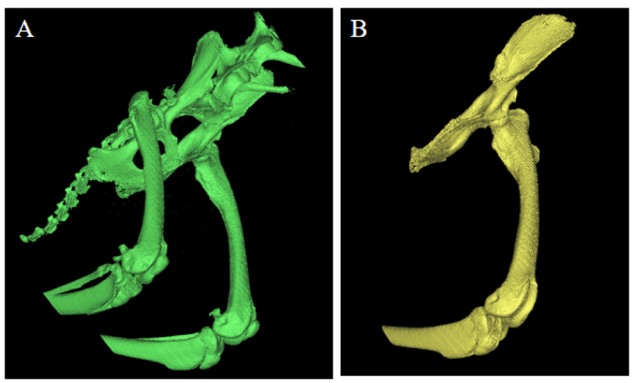

Fig. 5 (A) The structure of the rabbit's lower limbs was obtained by threshold segmentation. (B) The unilateral segment of the rabbit was obtained by region growth.

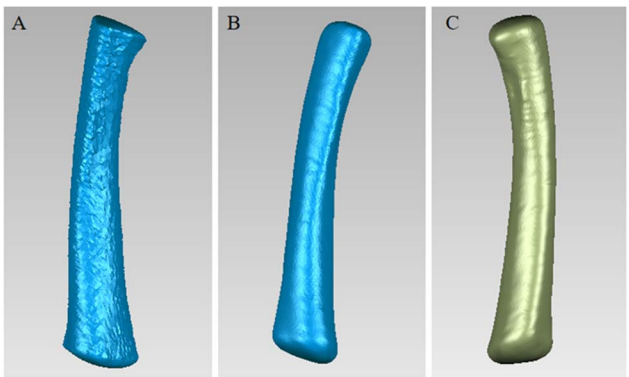

Fig. 6 Surface editing and optimization of 3D models. (A) Deletion of redundant pixels and filling of holes, (B) denoising and smoothing, and (C) accurate surface.

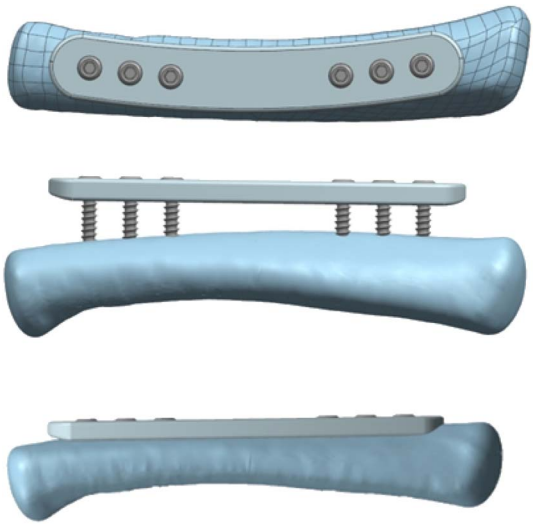

Fig. 7 Assembly of plate scaffold model and screw model.

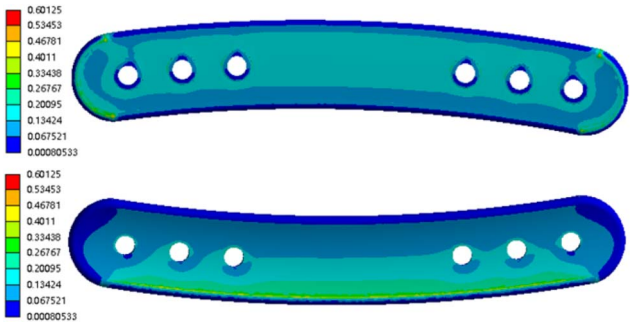

Fig. 8 Stress distribution of bone plate scaffold in finite element analysis.

responses. The stress distribution and concentration of the bone plate scaffold were mainly reflected in the ends and edges of the plate, which was consistent with the characteristics of stress distribution of the material when subjected to external force. And the maximum stress response of the femoral plate was 0.6 MPa, which was far away from the bending strength point of the PEEK material. This indicated that the PEEK bone plate scaffold prepared by this 3D model could meet the mechanical performance requirements when applied.

We examined the mechanical properties of the PEEK bone plate scaffold. In the three-point bending test, the four PEEK bone plate scaffold samples (PEEK 1, PEEK 2, PEEK 3, and PEEK 4) showed similar stress–strain curves (Fig. S2†). The maximum bending strength of the PEEK bone plate scaffold was 104.51 ± 0.31 MPa, and it began to show obvious plastic deformation after reaching the maximum stress at a strain of about 0.5%. At a strain of 2.5%, the stress of all samples tended to stabilize. The bending modulus of the PEEK bone plate scaffold was 5795.1 ± 704.5 MPa. The results showed that all samples showed good bending strength and plastic deformation capacity similar to other studies of PEEK bone plate scaffolds and were suitable for use in load-bearing applications.[27]

3.2 Micromorphology and crystal structure of bioactive bone plate scaffold

We prepared PEEK bone plate scaffolds according to the designed 3D bone plate model through FDM 3D printing technology. Furthermore, we used plasma spraying technology to apply bioactive coatings on the surface of PEEK bone plate scaffolds, including HA, Ta and Ti, to prepare HA-PEEK, Ta-PEEK and Ti-PEEK bioactive bone plate scaffolds. We used the fixture to limit the spraying area to the fracture area in the middle of the bone plate and added the porous structure to facilitate the adhesion and proliferation of osteoblasts (Fig. 9).[28]

Next, we further observed the microscopic morphology of the surface of PEEK bone plate scaffolds with different coatings by SEM. The SEM results showed that the surface of the 3D printed PEEK bone plate scaffold was smooth and flat regardless of the low or high magnification images, which was due to the suitable high-temperature printing process (Fig. 10). The surface of the bioactive bone plate scaffold showed uniformly dispersed spray powder and no obvious cracks, indicating the integrity of the coating. However, although the surface of the plasma sprayed bone plate scaffold was smoother in the low magnification image, the microscopic morphology with higher magnification showed the deposition of metal or ceramic powder particles of different shapes. These irregular particle depositions formed pore structures of different sizes and shapes. The surfaces of HA-PEEK and Ti-PEEK bone plate scaffolds showed stacked hydroxyapatite spherical particles and titanium spherical particles, which were similar to the surfaces of other plasma

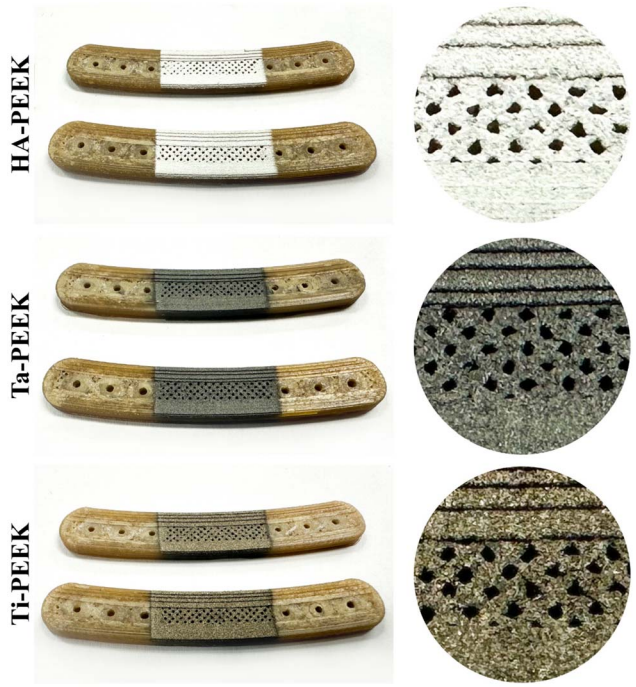

Fig. 9 Appearance and partial enlarged pictures of HA-PEEK, Ta-PEEK and Ti-PEEK plate scaffolds.

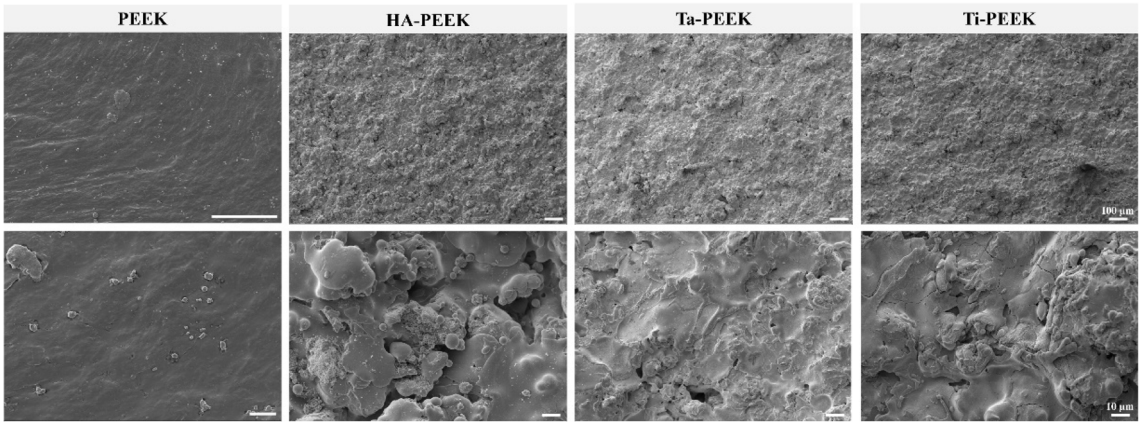

Fig. 10 The SEM images of PEEK, HA-PEEK, Ta-PEEK and Ti-PEEK bone plate scaffold.

sprayed coatings.[29] The surface of Ta-PEEK bone plate scaffold showed the irregular fluid states. These morphological differences are related to the melting points and properties of different materials. The rough coating microstructure and porous structure brought by plasma spraying technology are conducive to mimicking the complex structure of natural bone tissue.[30] Shao Jie *et al.* reported that a porous silica scaffold with a rough surface structure effectively promoted the adhesion and proliferation of bone marrow mesenchymal stem cells.[31]

Furthermore, we observed the element distribution on the surface of the bioactive bone plate scaffold. The HA-PEEK bone plate scaffold (Fig. 11A) showed a large amount of calcium (Ca) and phosphorus (P). The element ratio results (Fig. 11B and Table 3) showed that the HA-coating contained 31.10% oxygen (O), 48.06% calcium (Ca) and 16.47% phosphorus (P). The Ta-coating showed a large amount of tantalum and the element distribution was not uniform. However, the results of the element map (Fig. 11C and Table 3) showed that the mass ratio

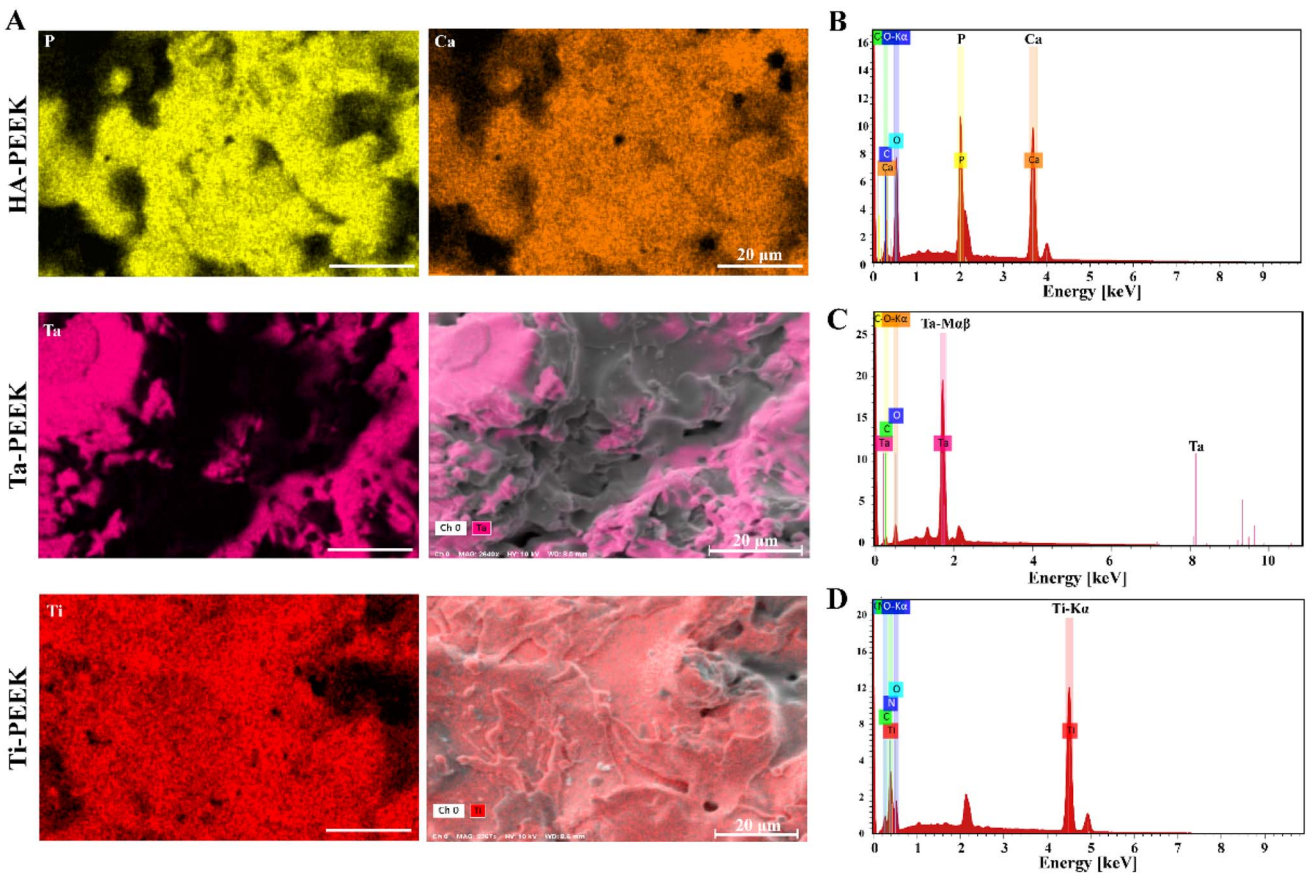

Fig. 11 (A) The EDS images of HA-PEEK, Ta-PEEK and Ti-PEEK bone plate scaffold. The EDS diagram of the (B) HA-PEEK, (C) Ta-PEEK and (D) Ti-PEEK bone plate scaffold.

Table 4 Percentage of HA-coating, Ta-coating and Ti-coating elements tested by EDX

Group	C (wt%)	O (wt%)	N (wt%)	Ca (wt%)	P (wt%)	Ta (wt%)	Ti (wt%)
HA-PEEK	4.37	31.10	—	48.06	16.47%	—	—
Ta-PEEK	6.68	9.76	—	—	—	83.56	—
Ti-PEEK	2.00	12.67	3.01	—	—	—	82.32

of Ta element reached 83.56%. Therefore, we inferred that the high melting point of Ta led to the uneven landing of the molten powder particles during the spraying process. The surface of the Ti-PEEK bone plate scaffold showed a lot of Ti elements with a content of 82.32% (Fig. 11D and Table 4). The relevant elements on the surface of the HA-PEEK and Ti-PEEK bone plate scaffolds were evenly distributed, which was also because the melting points of hydroxyapatite and Ti were similar and not too high. In addition, the surface of the Ti-PEEK bone plate scaffold presented 12.67% O element and 3.01% N element. The results indicated that nitrides and oxides might be formed during the spraying process.

Then, we examined the XRD spectra of PEEK bone plate scaffolds and bioactive coatings in the 2θ range. The XRD spectrum of PEEK (Fig. 12) showed the characteristic peaks of PEEK crystallization at $2\theta \approx 18.72°$, 20.66°, 22.6° and 28.58° and the broad hump of the amorphous phase, corresponding to the semi-crystalline structure of PEEK. The XRD results of HA-coating showed the characteristic peaks of the fingerprint region of HA at $2\theta \approx 31.8°$, 32.18° and 32.96°, indicating the successful deposition of hydroxyapatite. The HA coating has no characteristic peak at $2\theta \approx 64.2°$, which may be due to the conversion of part of the crystalline hydroxyapatite to amorphous state caused by plasma spraying.[32] The spectrum of the tantalum coating shows characteristic peaks at $2\theta \approx 23.06°$, 36.96°, 38.02°, 56.02° and 68.96°, indicating the presence of a mixture of metallic tantalum and its oxides, especially Ta_2O_5 and TaO_2.[33] This mixed phase may be caused by the high temperature of plasma spraying. The Ti-coating showed characteristic peaks of α-Ti at $2\theta \approx 62.3°$, 74.66° and 78.58°. The sharp α-Ti peak indicated a well-crystallized titanium coating. At the same time, the results also showed characteristic peaks of titanium oxide and titanium nitride,[29] which was consistent with the conclusion of EDS.[34] Jan Cizek *et al.*'s research showed that titanium nitride and titanium oxide were produced during the formation of Ti coating by plasma spraying.[35]

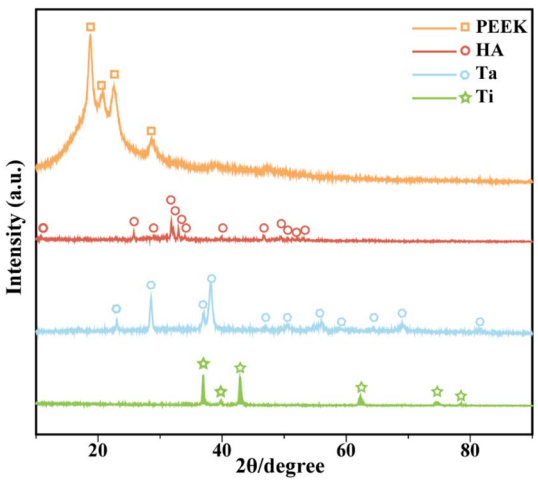

Fig. 12 XRD patterns of plasma sprayed Ta, HA, Ti coatings and PEEK plate scaffold.

3.3 Cytocompatibility of bioactive bone plate scaffold

To investigate the cytocompatibility of the bone plate scaffold, we tested the cytotoxicity of rBMSCs cultured in the bone plate scaffold for 1 day according to the international standard ISO10993-5. The CCK-8 results (Fig. 13A) showed that the cell viability of the PEEK bone plate scaffold was 93.86%, while that of the hydroxyapatite coating group was 95.41%, that of the tantalum coating group was 93.41%, and that of the titanium coating group was 99.40%. The cell viability of the PEEK bone

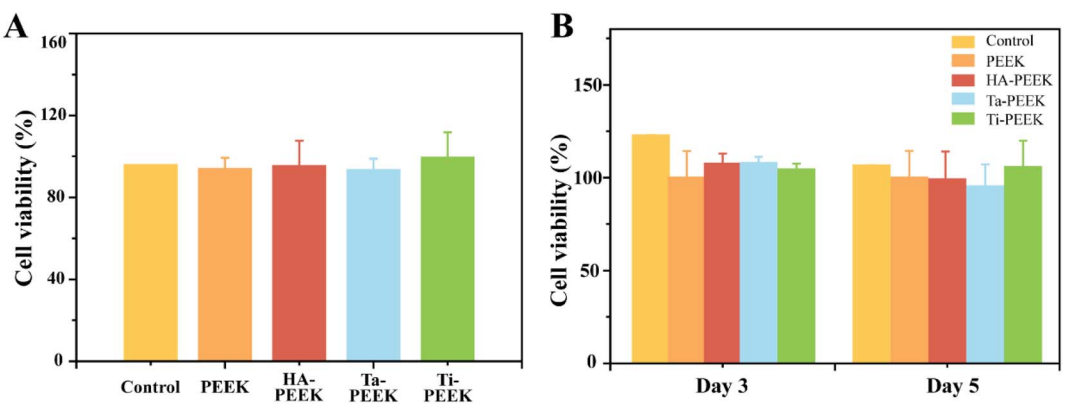

Fig. 13 Cell viability of rBMSCs cultured on bioactive bone plate scaffolds for (A) 1 day, (B) 3 and 5 days.

plate scaffold, whether coated or not, was greater than 90%, indicating that the bone plate scaffold had outstanding cell compatibility. Furthermore, we cultured for 3 and 5 days and tested the cell viability of rBMSCs. Compared with the results of 1 day and 5 days, the CCK-8 results of all groups on 3 days showed a slight increase (Fig. 13B). The cell viability in the PEEK bone plate scaffold was 100%, while that of the HA-PEEK group was 107.61%, that of the Ta-PEEK group was 107.98%, and that of the Ti-PEEK group was 104.55%. The cell viability of the bioactive bone plate scaffold was slightly higher than that of the bone plate scaffold. On 5 days, the cell viability of rBMSCs began to decrease slightly but it was still higher than that on the 1 day. Although the bioactive coating did not show a significant promotion of cell proliferation, it showed excellent cell compatibility, which was related to the relative inertness of PEEK material and the bioactivity of hydroxyapatite, titanium and tantalum.[10,12]

3.4 Osteogenic efficacy of bioactive bone plate scaffolds *in vitro*

To explore the osteogenic properties of the bone plate scaffolds, we further investigated the ALP and alizarin red expression of rBMSCs after 2 weeks of co-culture with the scaffold extract. The expression of ALP contributes to the availability of phosphate and mineral deposition, indicating that rBMSCs are transforming into osteoblasts.[36] The ALP staining results (Fig. 14A) showed that the rBMSCs in the HA-PEEK group showed the darkest blue among all groups. The statistical analysis results (Fig. 14D) also showed the highest ALP activity in the HA-PEEK group. The high-magnification images (Fig. 14C) showed that the bioactive bone plate scaffold groups all showed a larger area of ALP expression compared with the control group and the PEEK group. The ALP-expressing cytoplasm of the control group and the PEEK group was only granular and small spindle-shaped, while the rBMSCs in the other groups became elongated and formed nodular structures. In addition, alizarin red can specifically bind to calcium ions and stain the cap deposition area, indicating that rBMSCs mature into osteoblasts.[37] The results of alizarin red staining and statistical analysis (Fig. 14B and E) showed that the HA-PEEK group and the Ti-PEEK group presented more red calcium deposition areas, among which the red area of the HA-PEEK group was the largest. The red mineralized nodules were densely distributed around the cells, indicating the formation of mineralized matrix after HA-PEEK treatment. The statistical analysis results (Fig. 14E) showed that the red area of the bioactive bone plate scaffold group was significantly higher than that of the PEEK bone plate scaffold and the control group, indicating that the bioactive coating has an outstanding calcium deposition ability. Notably, whether ALP staining results or alizarin red staining results, the HA-PEEK bone plate scaffold showed outstanding osteogenic efficacy. Because the calcium ions and phosphate particles released by the degradation of hydroxyapatite promote bone mineralization and osteoblast differentiation.[38]

3.5 Evaluation of osteogenesis after implantation of bioactive bone plate scaffolds

We constructed a femoral defect model of New Zealand white rabbits and selected HA-PEEK and Ta-PEEK bioactive bone plate scaffolds that performed well *in vitro* osteogenesis experiments

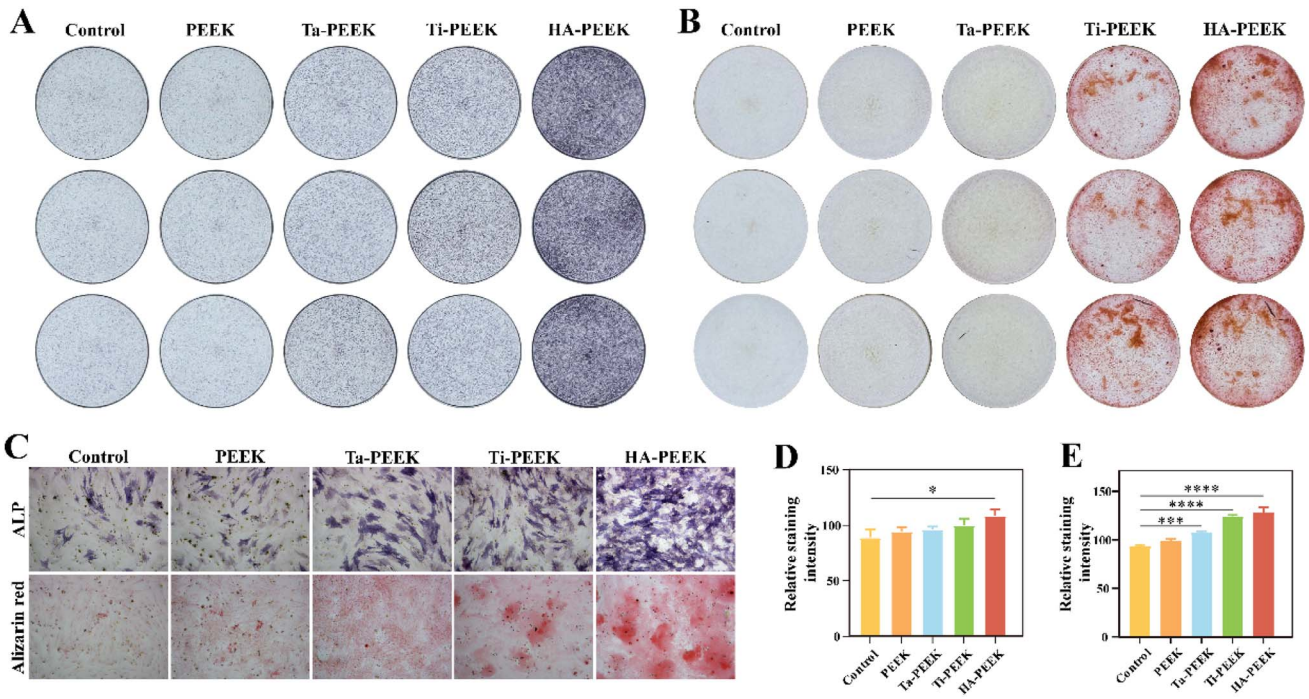

Fig. 14 (A) ALP staining, (B) alizarin red staining, and (C) high magnification images of rBMSCs after treatment with control, PEEK, Ta-PEEK, Ti-PEEK and HA-PEEK bioactive bone plate scaffolds. (D) and (E) Semi-quantitative statistics of ALP and alizarin red.

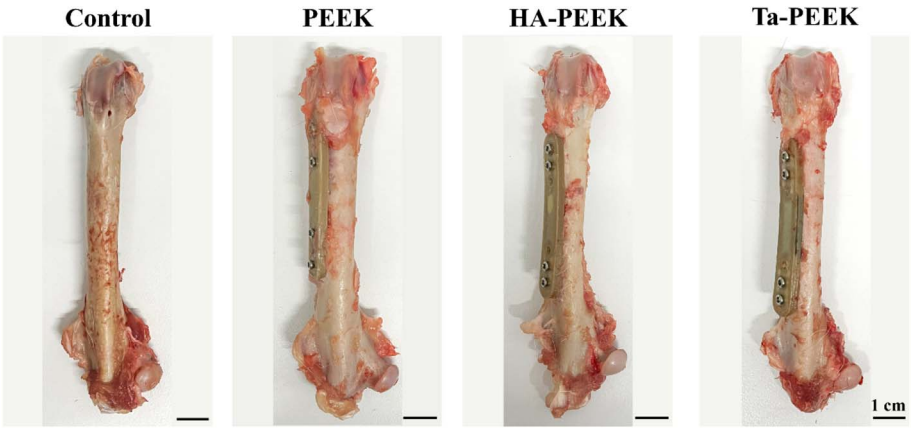

Fig. 15 Appearance of rabbit femur after 12 weeks of implantation of different bioactive bone plate scaffolds.

to further evaluate their osteogenesis performance. The 3D reconstruction image after scaffold implantation was shown in Fig. S3.† The bone plate scaffold customized according to the femoral sampling model fited the femoral curve perfectly. Although we reduced the number of screws to 4 during surgery, the plate and femur still fited perfectly. As shown in Fig. 15, 12 weeks after implantation, the bone plate scaffold was still well fixed to the femur without displacement or screw fall-off. These results indicated that the model we constructed was constructed by Geomagic Studio 12 software and the bone plate scaffold prepared based on it successfully.

In addition, to further observe the osteogenesis, we performed CT scanning and 3D reconstruction on the removed bone tissue at week 12. The untreated mid-femur showed the

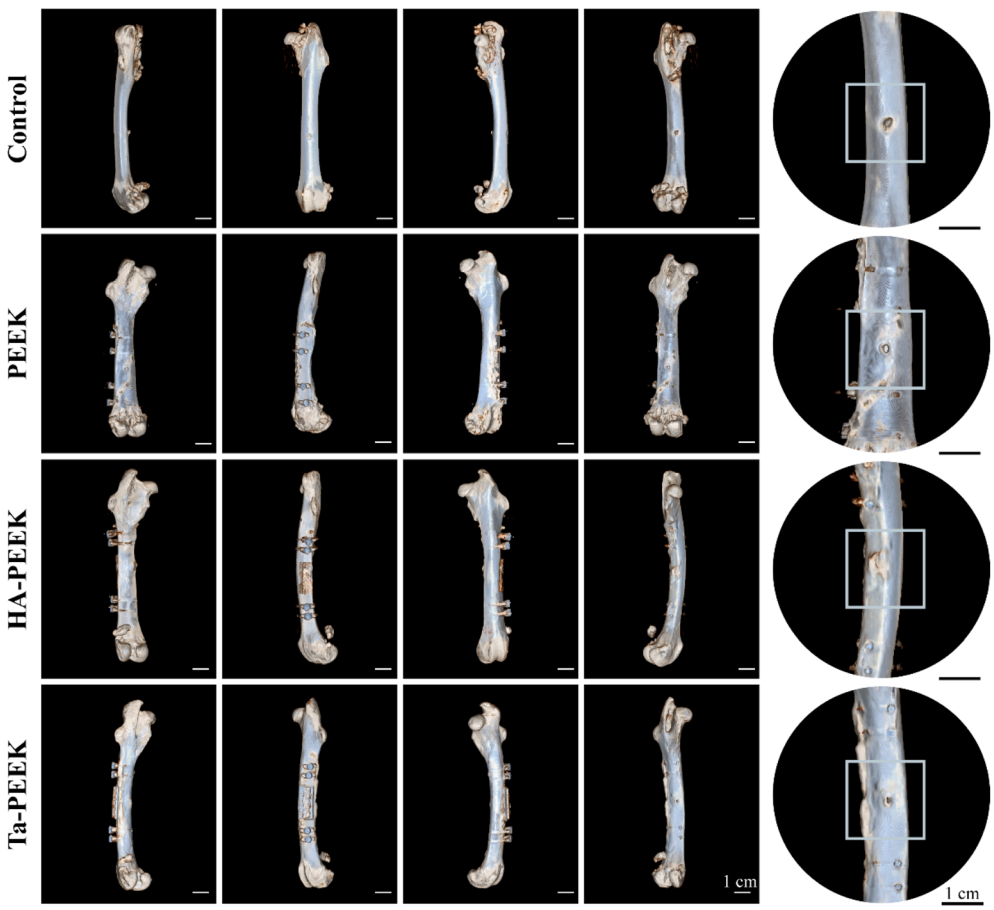

Fig. 16 3D reconstructed CT images (left, front, right and back views) of rabbit femurs with different bioactive bone plate scaffolds implanted at 12 weeks.

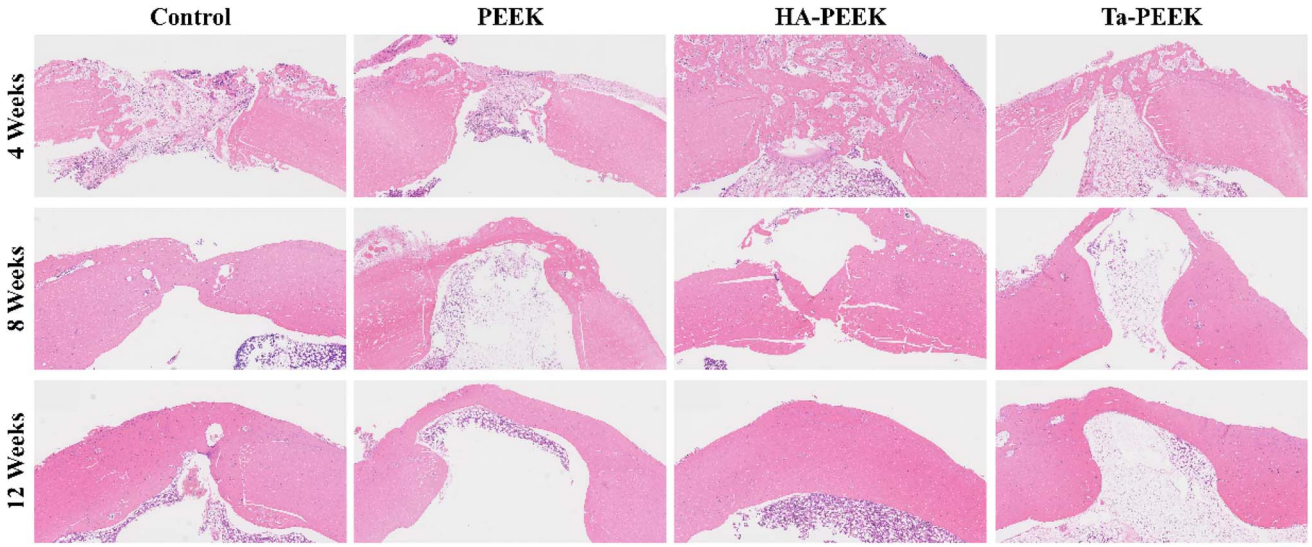

Fig. 17 H&E stained sections of bone tissue after treatment with different bioactive bone plate scaffolds at 4, 8, and 12 weeks.

largest circular perforated defect and the deepest defect area compared with the treated group (Fig. 16). This is because the defective femur lacked the fixation and mechanical support of the bone plate scaffold on the damaged bone segment.[39] The Ta-coated bone plate scaffold group showed an elongated oval defect compared with the uncoated PEEK bone plate scaffold group, indicating that the excellent osteoconductive properties of the Ta coating are conducive to the regeneration of bone tissue in the defect area.[40] Notably, the femoral defect area of the HA-PEEK group was completely covered by new bone tissue and there was no obvious gap and discontinuity in the defect area. The osteogenesis effect of the HA-PEEK bone plate scaffold was better than that of the Ta-PEEK, which is due to the osteoinductivity and bioabsorbability of the hydroxyapatite coating compared with the tantalum coating.[41]

Furthermore, we took femoral tissue for H&E staining and Masson staining to observe the tissue and cells at the defect site after bone plate scaffold treatment. At week 4, the defect area in each group was obviously bridged by osteoid and a large number of inflammatory cells appeared. The defect area in the control group was the largest (Fig. 17), while the HA-PEEK group showed the most osteoid deposition in the bone plate group. The inflammation in each group subsided and obvious osteoid bridging was shown at week 8. After HA-PEEK treatment, a more dense and orderly red bone matrix was formed at the defect site. At week 12, the bone gradually matured and the bone plate scaffold group showed complete bridging. The HA-PEEK group showed mature and orderly lamellar bone. The Masson staining results (Fig. 18) of each group showed a lighter blue color at week 4, indicating insufficient collagen deposition in the early

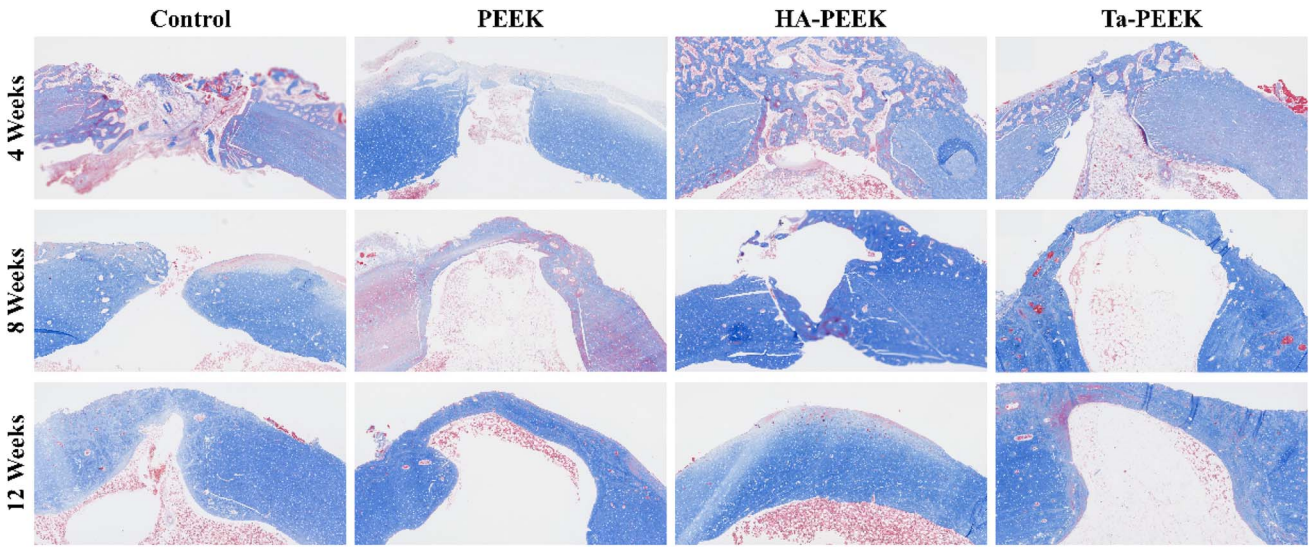

Fig. 18 Masson-stained sections of bone tissue after treatment with different bioactive bone plate scaffolds at 4, 8, and 12 weeks.

stage of bone formation. At week 8, the osteoid in the control group that was originally shown in H&E staining disappeared in the Masson staining section, indicating that this part of the osteoid was not fully mineralized. The bone plate scaffold groups all showed blue bridges corresponding to the collagen in mature mineralized bone. At week 12, the HA-PEEK group showed a clear layered structure and partially red mineralized bone tissue, which was similar to the bone repair performance of other HA-coated PEEK implants.[42] The bone regeneration rate in the PEEK group was slow and incomplete compared to the bioactive bone plate scaffold group, indicating that although the 3D printed bone plate scaffold provided effective mechanical support, it could not further stimulate bone healing. Notably, the HA-PEEK bone plate scaffold significantly accelerated bone tissue regeneration compared to the Ta-PEEK bone plate scaffold, because the hydroxyapatite coating on the surface of the scaffold promoted the osteogenic differentiation of rBMSCs and the expression of ALP, which was consistent with the results of the *in vitro* osteogenesis experiment.

4. Conclusion

Splinting is widely used for internal fixation in limb fractures, particularly for complex and displaced fractures, offering improved prognosis and reduced disability. This study developed a customized PEEK bone plate scaffold using CT data and 3D modeling techniques, ensuring precise anatomical fit and mechanical support, as confirmed by finite element analysis. Furthermore, we used PEEK material to 3D print the plate scaffolds by an FDM 3D printer and separately made HA-coated, Ta-coated, and Ti-coated plate scaffolds by plasma spraying technology. SEM results and EDS results showed that the surface of the bioactive bone plate scaffold was porous and distributed with corresponding metal elements, including calcium, phosphorus, tantalum, and titanium. The XRD results of each bone plate scaffold further exhibited the successful deposition of the bioactive coating. *In vitro* tests demonstrated the bioactive scaffolds' cytocompatibility and osteogenic properties, with HA-PEEK significantly enhancing ALP expression and calcium deposition in rBMSC. *In vivo* evaluations using a femoral defect model showed that HA-PEEK scaffolds promoted complete bone defect coverage and accelerated bone regeneration, outperforming other groups. In conclusion, the bioactive bone plate scaffold provides a potential strategy for the treatment of fractures in digital precision medicine.

Data availability

The data that support the findings of this study are available on request from the corresponding author upon reasonable request.

Author contributions

Wenquan Zhang: conceptualization, methodology, validation, investigation, data curation, writing – original draft, writing – review & editing, visualization. Dayou Shi: methodology, software, validation, investigation. Shirui Huang: software, formal analysis, visualization. Shaochuan Li: investigation, resources. Min Zeng: resources, data curation. Yanming Wei: conceptualization, writing – review & editing, supervision, project administration, funding acquisition.

Conflicts of interest

The authors declare no conflict of interest.

References

1 J. A. Cauley, The global burden of fractures, *Lancet Healthy Longevity*, 2021, **2**(9), e535–e536.
2 J. A. Baron, J. A. Barrett and M. R. Karagas, The epidemiology of peripheral fractures, *Bone*, 1996, **18**(3), S209–S13.
3 S. Amin, S. J. Achenbach, E. J. Atkinson, *et al.*, Trends in Fracture Incidence: A Population-Based Study Over 20 Years, *J. Bone Miner. Res.*, 2013, **29**(3), 581–589.
4 J. N. Farr, L. J. Melton III, S. J. Achenbach, *et al.*, Fracture Incidence and Characteristics in Young Adults Aged 18 to 49 Years: A Population-Based Study, *J. Bone Miner. Res.*, 2017, **32**(12), 2347–2354.
5 N. Dehghan and M. D. Mckee, What's New in Orthopaedic Trauma, *J. Bone Jt. Surg.*, 2020, **102**(13), 2823–2838.
6 J. Li, L. Qin, K. Yang, *et al.*, Materials evolution of bone plates for internal fixation of bone fractures: A review, *J. Mater. Sci. Technol.*, 2020, **36**, 190–208.
7 H. Uhthoff and M. Finnegan, The effects of metal plates on post-traumatic remodelling and bone mass, *J. Bone Jt. Surg., Br. Vol.*, 1983, **65**(1), 66–71.
8 D. Savio and A. Bagno, When the Total Hip Replacement Fails: A Review on the Stress-Shielding Effect, *Processes*, 2022, **10**(3), 612.
9 S. Samiezadeh, P. Tavakkoli Avval, Z. Fawaz, *et al.*, On optimization of a composite bone plate using the selective stress shielding approach, *J. Mech. Behav. Biomed. Mater.*, 2015, **42**, 138–153.
10 S. Mishra and R. Chowdhary, PEEK materials as an alternative to titanium in dental implants: A systematic review, *Clin. Implant Dent. Relat. Res.*, 2019, **21**(1), 208–222.
11 S. Verma, N. Sharma, S. Kango, *et al.*, Developments of PEEK (Polyetheretherketone) as a biomedical material: A focused review, *Eur. Polym. J.*, 2021, **147**, 110295.
12 S. M. Kurtz and J. N. Devine, PEEK biomaterials in trauma, orthopedic, and spinal implants, *Biomaterials*, 2007, **28**(32), 4845–4869.
13 P. Sikder, B. T. Challa and S. K. Gummadi, A comprehensive analysis on the processing-structure-property relationships of FDM-based 3-D printed polyetheretherketone (PEEK) structures, *Materialia*, 2022, **22**, 101427.
14 R. B. Kristiawan, F. Imaduddin, D. Ariawan, *et al.*, A review on the fused deposition modeling (FDM) 3D printing: Filament processing, materials, and printing parameters, *Open Eng.*, 2021, **11**(1), 639–649.
15 P. Wang, B. Zou, H. Xiao, *et al.*, Effects of printing parameters of fused deposition modeling on mechanical

properties, surface quality, and microstructure of PEEK, *J. Mater. Process. Technol.*, 2019, **271**, 62–74.
16 H.-J. Chung, H.-B. Lee, K.-M. Park, *et al.*, Feasibility of 3D-Printed Locking Compression Plates with Polyether Ether Ketone (PEEK) in Tibial Comminuted Diaphyseal Fractures, *Polymers*, 2023, **15**(14), 3057.
17 T. Kim, C. W. See, X. Li, *et al.*, Orthopedic implants and devices for bone fractures and defects: Past, present and perspective, *Eng. Regener.*, 2020, **1**, 6–18.
18 S. Li, T. Wang, J. Hu, *et al.*, Surface porous poly-ether-ether-ketone based on three-dimensional printing for load-bearing orthopedic implant, *J. Mech. Behav. Biomed. Mater.*, 2021, **120**, 104561.
19 F. Suska, O. Omar, L. Emanuelsson, *et al.*, Enhancement of CRF-PEEK osseointegration by plasma-sprayed hydroxyapatite: A rabbit model, *J. Biomater. Appl.*, 2014, **29**(2), 234–242.
20 W. R. Walsh, N. Bertollo, C. Christou, *et al.*, Plasma-sprayed titanium coating to polyetheretherketone improves the bone-implant interface, *Spine J.*, 2015, **15**(5), 1041–1049.
21 K.-J. Cheng, Z.-Y. Shi, R. Wang, *et al.*, 3D printed PEKK bone analogs with internal porosity and surface modification for mandibular reconstruction: An in vivo rabbit model study, *Biomater. Adv.*, 2023, **151**, 213455.
22 B. I. Oladapo, S. A. Zahedi, S. O. Ismail, *et al.*, 3D printing of PEEK–cHAp scaffold for medical bone implant, *Bio-Des. Manuf.*, 2021, **4**(1), 44–59.
23 F. Manzoor, A. Golbang, S. Jindal, *et al.*, 3D printed PEEK/HA composites for bone tissue engineering applications: Effect of material formulation on mechanical performance and bioactive potential, *J. Mech. Behav. Biomed. Mater.*, 2021, **121**, 104601.
24 L. R. Huff, P. A. Taylor, J. Jani, *et al.*, Proximal humeral fracture fixation: a biomechanical comparison of two constructs, *J. Shoulder Elb. Res.*, 2013, **22**(1), 129–136.
25 M. Fedel, V. Micheli, M. Thaler, *et al.*, Effect of nitrogen plasma treatment on the crystallinity and self-bonding of polyetheretherketone (PEEK) for biomedical applications, *Polym. Adv. Technol.*, 2020, **31**(2), 240–247.
26 X.-R. Zhu, C. Chen, Y.-W. Hua, *et al.*, A comparative quantitative assessment of 3D-printed PEKK and PEEK thin meshes in customized alveolar bone augmentation, *BMC Oral Health*, 2024, **24**(1), 1304.
27 J. Sun, J. Li, A. Shan, *et al.*, A novel multifunctional PEEK internal fixation plate regulated by Gentamicin/chitosan coating, *Colloids Surf., B*, 2025, **245**, 114316.
28 M. Mastrogiacomo, S. Scaglione, R. Martinetti, *et al.*, Role of scaffold internal structure on in vivo bone formation in macroporous calcium phosphate bioceramics, *Biomaterials*, 2006, **27**(17), 3230–3237.
29 F. Sargin, G. Erdogan, K. Kanbur, *et al.*, Investigation of in vitro behavior of plasma sprayed Ti, TiO2 and HA coatings on PEEK, *Surf. Coat. Technol.*, 2021, **411**, 126965.
30 S. Bose, S. Vahabzadeh and A. Bandyopadhyay, Bone tissue engineering using 3D printing, *Mater. Today*, 2013, **16**(12), 496–504.
31 S.-J. Wang, D. Jiang, Z.-Z. Zhang, *et al.*, Biomimetic Nanosilica–Collagen Scaffolds for In Situ Bone Regeneration: Toward a Cell-Free, One-Step Surgery, *Adv. Mater.*, 2019, **31**(49), 1904341.
32 L. Major, D. F. Kopp, R. Major, *et al.*, Microstructural and micromechanical characteristics of composite osteoconductive coatings deposited by the atmospheric pressure plasma technique, *J. Microsc.*, 2024, **295**(2), 177–190.
33 F. Wang, C. Li, S. Zhang, *et al.*, Tantalum coated on titanium dioxide nanotubes by plasma spraying enhances cytocompatibility for dental implants, *Surf. Coat. Technol.*, 2020, **382**, 125161.
34 S. Cassaignon, M. Koelsch and J.-P. Jolivet, From TiCl3 to TiO2 nanoparticles (anatase, brookite and rutile): Thermohydrolysis and oxidation in aqueous medium, *J. Phys. Chem. Solids*, 2007, **68**(5), 695–700.
35 J. Cizek, O. Kovarik, J. Siegl, *et al.*, Influence of plasma and cold spray deposited Ti Layers on high-cycle fatigue properties of Ti6Al4V substrates, *Surf. Coat. Technol.*, 2013, **217**, 23–33.
36 H. Long, B. Sun, L. Cheng, *et al.*, miR-139-5p Represses BMSC Osteogenesis via Targeting Wnt/β-Catenin Signaling Pathway, *DNA Cell Biol.*, 2017, **36**(8), 715–724.
37 A. Bernar, J. V. Gebetsberger, M. Bauer, *et al.*, Optimization of the Alizarin Red S Assay by Enhancing Mineralization of Osteoblasts, *Int. J. Mol. Sci.*, 2023, **24**(1), 723.
38 D.-W. Zhao, M.-Z. Yu, Y.-X. Zhao, *et al.*, Improvement of bone formation by bionic hydroxyapatite nanorod via the regulation of macrophage polarization, *J. Mater. Sci. Technol.*, 2023, **136**, 109–120.
39 J. D. Boerckel, Y. M. Kolambkar, H. Y. Stevens, *et al.*, Effects of in vivo mechanical loading on large bone defect regeneration, *J. Orthop. Res.*, 2012, **30**(7), 1067–1075.
40 X. Wei, D. Zhao, B. Wang, *et al.*, Tantalum coating of porous carbon scaffold supplemented with autologous bone marrow stromal stem cells for bone regeneration in vitro and in vivo, *Exp. Biol. Med.*, 2016, **241**(6), 592–602.
41 K. Zhou, X. Wang, S. Han, *et al.*, Preparation and Biological Evaluation of Porous Tantalum Scaffolds Coated with Hydroxyapatite, *ACS Appl. Bio Mater.*, 2024, 6780–6790.
42 J. H. Lee, H. L. Jang, K. M. Lee, *et al.*, In vitro and in vivo evaluation of the bioactivity of hydroxyapatite-coated polyetheretherketone biocomposites created by cold spray technology, *Acta Biomater.*, 2013, **9**(4), 6177–6187.